PHYSICAL REVIEW E **73**, 041921 (2006)

Monte Carlo simulations of polyelectrolytes inside viral capsids

Daniel George Angelescu,[1,*] Robijn Bruinsma,[2] and Per Linse[1]
[1]*Physical Chemistry 1, Lund University, Box 124, SE-221 00 Lund, Sweden*
[2]*Department of Physics and Astronomy, UCLA, Box 951547, Los Angeles, California 90095-1547, USA*

(Received 7 December 2005; revised manuscript received 1 March 2006; published 18 April 2006)

Structural features of polyelectrolytes as single-stranded RNA or double-stranded DNA confined inside viral capsids and the thermodynamics of the encapsidation of the polyelectrolyte into the viral capsid have been examined for various polyelectrolyte lengths by using a coarse-grained model solved by Monte Carlo simulations. The capsid was modeled as a spherical shell with embedded charges and the genome as a linear jointed chain of oppositely charged beads, and their sizes corresponded to those of a scaled-down $T=3$ virus. Counterions were explicitly included, but no salt was added. The encapisdated chain was found to be predominantly located at the inner capsid surface, in a disordered manner for flexible chains and in a spool-like structure for stiff chains. The distribution of the small ions was strongly dependent on the polyelectrolyte-capsid charge ratio. The encapsidation enthalpy was negative and its magnitude decreased with increasing polyelectrolyte length, whereas the encapsidation entropy displayed a maximum when the capsid and polyelectrolyte had equal absolute charge. The encapsidation process remained thermodynamically favorable for genome charges ca. 3.5 times the capsid charge. The chain stiffness had only a relatively weak effect on the thermodynamics of the encapsidation.

DOI: 10.1103/PhysRevE.73.041921 PACS number(s): 87.15.Aa, 82.70.−y

I. INTRODUCTION

The structural organization of viruses is characterized by simplicity and economy. At a minimal level, the viral genome, which is composed of a number of RNA or DNA molecules that are either single stranded (ss) or double stranded (ds), is surrounded by a spherical or cylindrical protein shell composed of many copies of almost identical proteins. The linear size of the virus genome can be tens of microns and is large compared to the diameter of capsid, usually in the range of tens of nanometers, so the genome must undergo a high degree of condensation during viral assembly. The condensation scenario and the resulting structural organization of viral genomes can approximately be divided in two groups.

The capsids of viruses with ssRNA genomes—such as the polio and hepatitis B viruses—*require* the presence of genomic RNA molecules for efficient assembly, at least under physiological conditions [1]. The genome is encapsidated during assembly. The thermodynamic drive for this "coassembly" process is the strong electrostatic affinity of the negatively charged RNA molecules for the positively charged capsid proteins. The outer layer of the genome that is in contact with the surrounding capsid in fact adopts to a certain amount the icosahedral symmetry of the protein shell, presumably as a consequence of this affinity [2,3]. The interior of the genome, on the other hand, appears to be structurally isotropic with a region of reduced density at the center [4–7]. This nucleoprotein electrostatic affinity must be able to overcome the electrostatic self-repulsion of the genome that will resist genome compaction. This genomic self-repulsion is expected to lead to an enhanced pressure inside a virus.

The importance of the electrostatic interactions for viruses was first deduced from the fact that the spontaneous assembly of a viral particle under *in vitro* conditions from an aqueous solution with viral proteins and viral RNA molecules—discovered in 1955 by Fraenkel-Conrat and Williams—only proceeds over a certain salinity range and for certain salt compositions [8]. The virus formation free energy has recently been measured by thermodynamic means, and the law of mass action has been applied for hepatitis B virus [9] and the cowpea chlorotic mottle virus (CCMV) [10]. The dependence on solution salinity of the formation free energy ($\approx 10^3 kT$) confirmed the electrostatic origin of coassembly. The capsid surface charge density obtained from a fit to experimental data was found to be almost one net electrical charge per nm^2, which agrees reasonably well with the nominal "chemical" charge of the typical capsid proteins [11].

The assembly process of viruses with dsDNA genomes, such as that of the bacteriophage viruses or the herpes virus, follows a rather different route. The capsid is assembled first. The genome does not play an essential role in capsid assembly and is afterwards inserted into the preformed capsids by the action of a powerful molecular motor imbedded in the capsid.

A key physical difference between ssRNA and dsDNA genomes in this respect is the bending rigidity. Double-stranded DNA genomes have a persistence length of the order of 50 nm, which is large compared to the size of the capsid, whereas ssRNA (or ssDNA) strands have persistence lengths of the order of a nanometer. The genome of the phage viruses and of herpes has a spool-like organization, again with a low-density hole at the center, and exhibits no trace of the capsid icosahedral symmetry [12–19]. Theoretical studies

---

[*] Permanent address: Romanian Academy, Institute of Physical Chemistry "I. G. Murgulescu," Splaiul Independentei 202, 060021 Bucharest, Romania.

based on the wormlike chain (WLC) model of DNA [20–23], have confirmed that compaction of a stiff linear chain into spherical cavity leads to a spool-like structure. Finally, both thermodynamic [20,22,24,25] and micromechanical [26,27] studies of the genome compaction by phages report that a significant amount of positive external work must be performed during DNA compaction. The pressure exerted on the capsids of the phages has been measured as well and was found to be [28,29]. Theoretical studies indicate that this pressure is primarily due to electrostatic self-repulsion of the dsDNA [21,30,31]. Measurements of the pressure inside ssRNA viruses have not yet been carried out. A theoretical study of electrostatic coassembly of capsid proteins with generic linear polyelectrolytes, using mean-field theory, found that the pressure should be practically zero in this case [32].

A number of computer simulation studies have addressed the genome conformation within the capsid interior [20,25,33–37]. In particular, spool-like arrangements of dsDNA were investigated, based on diffraction [12] and electron microscopy [16,17] studies of the bacteriophage and herpes viruses. The simulation studies were carried out on model genomes consisting of linear chains of hard spheres (beads). Although typical bacteriophages have icosahedral capsids, the confining capsid was mostly modeled as an uncharged sphere. A more detailed capsid model was recently considered by Zhang *et al.* [37], who calculated the electrostatic potential of CCMV capsid in the absence and in the presence of N-terminal residues, which was then adopted to find the distribution of ssRNA with low energy. Despite the fundamental importance of the electrostatic interaction for viral assembly, the electrostatic interaction was excluded [20,33,35], or included only either as a short-range bead-bead repulsion of the Debye-Hückel (DH) type [36] or as a self-attraction using a Lennard-Jones potential representing the electrostatic cohesive effects appearing in the presence of multivalent counterions [20]. The linearization in the DH theory is questionable due to the large surface charge density of the capsid and the large linear charge density of the genome.

Charged macromolecules, such as charged colloids and polyelectrolytes (e.g., RNA and DNA), and their counterions are electrostatically attracted to each other. In solution, the competition between this attraction and the counteracting mixing entropy give rise to a diffuse layer of counterions near the macromolecules. When two oppositely charged macromolecules are brought close to each other in solution, the free energy of the system is generally reduced. This form of association of charged macromolecules is characterized enthalpically by a reduced electrostatic energy and entropically by a release of the counterions [38].

In the present paper, we present the results of a Monte Carlo study of a model system for the nucleoprotein coassembly driven by electrostatic interactions. Our approach involves a coarse-grained model; however, the electrostatics is treated in full detail, including the presence of the small ions. The aims of the study are to investigate the genome conformation as well as the encapsidation free energy and its dependence on the genome size and genome flexibility. In particular, we wanted to address questions such as the maximum genome size that could be compacted without external work. The capsid was modeled as a spherical shell with embedded charges and the genome as a linear jointed chain of oppositely charged beads. Capsid and genome sizes nominally correspond to those of a scaled-down $T=3$ virus such as CCMV. Counterions for both the capsid and the genome were explicitly present, but we did not include additional salt.

Our main findings can be summarized as follows. The encapisdated chain was located at the inner capsid surface. For low intrinsic stiffness, the chain configuration was essentially laterally disordered, while with increasing stiffness the chain adopted a spool-like structure. For undercharged capsids (genome charge less than that of the capsid) and for moderately overcharged capsids (genome charge at most twice that of the capsid) encapsidation is favored both enthalpically and entropically. The entropy increase is due to a net release of small ions. For more strongly overcharged capsids (genome charge larger than twice that of the capsid) encapsidation still is enthalpically favored, but entropically disfavored. When the genome charge exceeds ca. 3.5 times that of the capsid, the entropy penalty becomes larger than the enthalpy gain and the encapsidation ceases to be thermodynamic favorable.

II. MODEL AND METHODS

A. Model system

A coarse-grained model has been adopted to examine generic features of a polyelectrolyte-containing viral capsid and the thermodynamics of the encapsidation of the polyelectrolyte into the viral capsid with the $T=3$ phage as a template. The capsid of the $T=3$ phage has an icosahedral shape with a net positive charge, predominantly localized near the inner surface.

The viral capsid is modeled as a homogeneous spherical shell with imbedded monovalent positive charges. The shell has an inner radius $R_c=50$ Å and a thickness $D_c=12$ Å. The number of capsid charges is maintained at the fixed value $N_c=250$ with the charges positioned at the radial distance of 2 Å from the inner surface. One charge is located at each of the two poles with the remainder placed along 19 parallel circles. The curvilinear distance between successive charges on each circle is maintained at a contained value equal to the curvilinear distance between adjoining circles to achieve a near-uniform surface charge density. The polyelectrolyte is modeled as a linear, charged bead-spring chain with monovalent negatively charged beads. The beads are represented as hard spheres and joined by a harmonic bond potential. The intrinsic chain stiffness is regulated by including a harmonic bond-bond angular potential. The spherical shell is assumed to be impenetrable to the beads. Finally, both negatively and positively charged monovalent counterions that separately neutralized the charges of the two polyelectrolytes are included. The small ions are modeled as charged hard spheres, each bearing one unit charge. Unlike the polyelectrolyte beads, the small ions are allowed to pass across the capsid. The solvent and shell are treated as dielectric continua with constant relative permittivity. The model thus contains in total four different types of particles, viz., (i) the positively

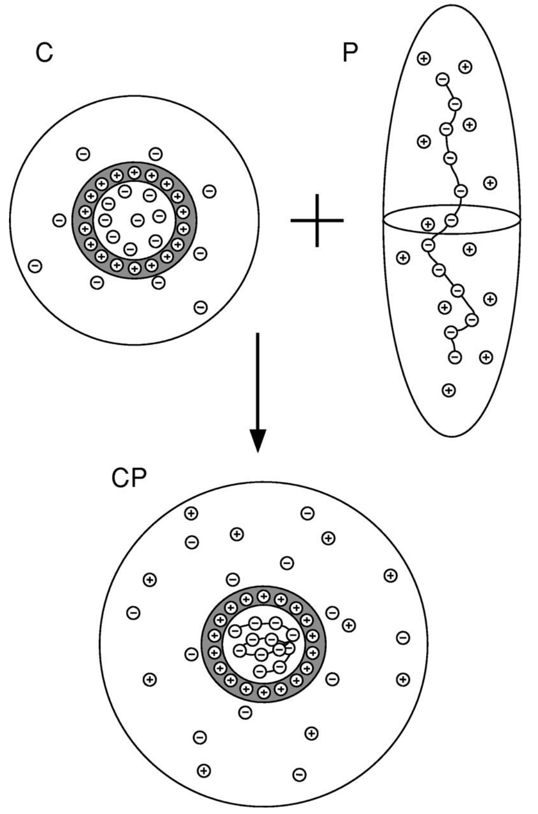

FIG. 1. Schematic illustration of the encapsidation process with the initial state composed of separated polyelectrolyte-free capsid (C) and polyelectrolyte (P) solutions and the final state of a polyelectrolyte-containing capsid solution (CP). The capsid and polyelectrolyte counterions are also displayed, and the shaded areas with embedded charges denote the capsid. Note, objects are not depicted to scale.

charged capsid, (ii) the negatively charged beads of the polyelectrolyte, (iii) the capsid counterions, and (iv) and the polyelectrolyte counterions.

The thermodynamics of the encapsidation process is examined by considering the transition between two states. The initial state comprises separated solutions of a polyelectrolyte-free capsid with its counterions (labeled C) and the polyelectrolyte and its counterions (labeled P), while the final state involves a solution of the encapsidated polyelectrolyte and the small ions (labeled CP); see Fig. 1. The cell approximation is used to describe the different solutions. In this approach, one or more polyions (e.g., the capsid, the polyelectrolyte, or both) plus the neutralizing counterions are placed in a cell having a hard wall with a shape appropriate for the polyion and a volume reflecting the polyion number density. A spherical cell is used for solutions containing the polyelectrolyte-free capsid or the encapsidated polyelectrolyte solution, whereas a prolate-shaped cell is used for the polyelectrolyte solution. In Appendix A, we discuss in more detail the selection of the prolate geometry for the polyelectrolyte solution. The cell approach is known to be a useful simplification to examine systems possessing correlations over different length scales [39].

The values of the parameters used in the present work and data of the $T=3$ phage are summarized in Table I. Although the dimensions of the model correspond approximately to those of a $T=3$ phage virus, this model is of course by no means a realistic description of a $T=3$ virus. First of all, the model does not include any molecular-level structural details of the polyelectrolyte or the capsid proteins nor does it reflect the icosahedral symmetry of the capsid. Actual viral ssRNA polyelectrolytes have a branched secondary structure that we are not including. Even a small $T=3$ virus has a capsid charge of about +2000 and a polyelectrolyte charge of about −4500, ca. one order of magnitude larger than considered here. We also do not examine the possibly important role of added salt. Our aim is however to examine a model system that could be used as a testing ground for analytical theories of the thermodynamics of viral coassembly driven by the nucleoprotein electrostatic affinity that included the electrostatic self-repulsion of the polyelectrolyte and the bending stiffness of the polyelectrolyte, both of which resist viral assembly.

B. Interaction potentials

The total energy U of a C, P, or CP solution is expressed as a sum

$$U = U_{\text{nonbond}} + U_{\text{bond}} + U_{\text{angle}} + U_{\text{cell}}. \tag{1}$$

The nonbonding term U_{nonbond} is the sum of two contributions

$$U_{\text{nonbond}} = \sum_{i<j} u_{ij}(r_{ij}) + \sum_{i} u_{\text{c},i}(r_i). \tag{2}$$

The first contribution represents the hard-sphere and Coulomb interactions between charged beads according to

$$u_{ij}(r_{ij}) = \begin{cases} \infty, & r_{ij} < R_i + R_j, \\ \dfrac{Z_i Z_j e^2}{4\pi\varepsilon_0\varepsilon_{\text{r}} r_{ij}}, & r_{ij} \geqslant R_i + R_j, \end{cases} \tag{3}$$

where i and j denote either a polyelectrolyte bead or a small ion. Moreover, R_i is the hard-sphere radius of particle i, Z_i the valence of particle i, r_{ij} the distance between centers of the particles i and j, ε_0 the dielectric permittivity of the vacuum, and ε_r the relative permittivity of the aqueous medium. The second term of Eq. (2) represents the interaction between the mobile particles and the capsid charges according to

$$u_{\text{c},i}(r_i) = \begin{cases} \infty, & R_{\text{c}} - R_i < r_i < R_{\text{c}} + D_{\text{c}} + R_i, \\ \displaystyle\sum_{j=1}^{N_{\text{c}}} \frac{Z_i Z_j e^2}{4\pi\varepsilon_0\varepsilon_{\text{r}} |\mathbf{r}_i - \mathbf{r}_j|} & \text{otherwise}. \end{cases} \tag{4}$$

Here $\mathbf{r}_i$ denotes the position of particle i (polyelectrolyte bead or small ion) and $\mathbf{r}_j$ the position of capsid charge j.

The second term of Eq. (1), the bond energy U_{bond}, is given by

TABLE I. Data of the simulated systems and the main characteristics of the $T=3$ phage.

Variable	Symbol	Model	$T=3$ virus
Capsid			
Capsid inner radius	R_c	50 Å	100 Å
Capsid thickness	D_c	12 Å	25 Å
No. of capsid charges	N_c	250	~2000–2300
Capsid charge	Z_c	+1	+1
Anion charge		−1	−1
Anion radius		2 Å	
Polyelectrolyte			
No. of polyelectrolyte beads	N_b	100, 250, 400	≈4500
Bead charge	Z_b	−1	−1
Bead radius	R_b	2 Å	
Bead separation	$\langle R_{\mathrm{bb}}^2\rangle^{1/2}$	5–6 Å	5.6 Å
Bare persistence length	l_p^0	8.5, 50, 550 Å	
Cation charge		+1	+1
Cation radius		2 Å	
Simulation cells (structure analysis)			
Radius of sphere[a]	R_{cell}	100–1000 Å	
Radius of sphere[b]	R_{cell}	500.0, 563.1, 614.6 Å	
Simulation cells (polyelectrolyte encapsidation)			
Radius of sphere[a]	R_{cell}	427.5 Å	
Minor axes of prolate[c]	R_x, R_y	250 Å	
Major axis of prolate[c]	R_z	750, 1875, 3000 Å[d]	
Radius of sphere[b]	R_{cell}	[e]	

[a] Spherical cell used for the polyelectrolyte-free capside solution.

[b] Spherical cell used for the polyelectrolyte-containing capsid solution.

[c] Prolate-shaped cell used for the polyelectrolyte solution.

[d] Adjusted to a bead number density $\rho_b=5.11\times10^{-7}$ Å^{-3}.

[e] Adjusted to give $V_{\mathrm{CP}}=V_{\mathrm{C}}+V_{\mathrm{P}}$ (see text).

$$U_{\mathrm{bond}}=\sum_{i=1}^{N_b-1}\frac{k_{\mathrm{bond}}}{2}(r_{i,i+1}-r_0)^2 \qquad (5)$$

where N_b is the number of polyelectrolyte beads, $r_{i,i+1}$ the distance between two adjacent beads in the chain, r_0 the equilibrium bond distance ($r_0=5$ Å), and k_{bond} the bond force constant ($k_{\mathrm{bond}}=0.4$ N m^{-1}). At room temperature, a thermal average gives for the root-mean-square (rms) bead-bead separation $\langle R_{\mathrm{bb}}^2\rangle^{1/2}\approx 5.5$–$6.0$ Å. Next, the bond-bond angular potential energy U_{angle} of Eq. (1) is given by

$$U_{\mathrm{angle}}=\sum_{i=2}^{N_b-1}\frac{k_{\mathrm{angle}}}{2}(\alpha_i-\alpha_0)^2 \qquad (6)$$

where α_i is the angle between the vectors $\mathbf{r}_{i+1}-\mathbf{r}_i$ and $\mathbf{r}_{i-1}-\mathbf{r}_i$ that connect the ith bead with the two neighboring beads, α_0 the equilibrium angle ($\alpha_0=180°$), and k_{angle} the angular force constant.

Finally, the term U_{cell} in Eq. (1) describes the confining cell potential. It is given by

$$U_{\mathrm{cell}}=\sum_i u_{\mathrm{cell}}(r_i) \qquad (7)$$

with

$$u_{\mathrm{cell}}(r_i)=\begin{cases}\infty, & (x_i/R_x)^2+(y_i/R_y)^2+(z_i/R_z)^2>1,\\ 0, & (x_i/R_x)^2+(y_i/R_y)^2+(z_i/R_z)^2\leqslant 1,\end{cases} \qquad (8)$$

where x_i, y_i, and z_i are the Cartesian coordinates of particle i and R_x, R_y, and R_z the lengths of the semiaxes of the prolate cell. For the case of a spherical cell, $R_x=R_y=R_z\equiv R_{\mathrm{cell}}$.

C. Systems investigated

We examined the encapsidation of nine different polyelectrolytes by considering (i) three polyelectrolyte lengths and (ii) three intrinsic chain flexibilities. The different polyelectrolyte lengths are obtained by using $N_b=100$, 250, and 400 beads. The ratio β of the polyelectrolyte and capsid charges is an important parameter in this context,

$$\beta \equiv \frac{|N_b Z_\mathrm{b}|}{|N_\mathrm{c} Z_\mathrm{c}|} \tag{9}$$

with $|N_\mathrm{c} Z_\mathrm{c}|=250$. Thus, the case $N_b=100$ corresponds to $\beta < 1$ (undercharged capsid), $N_b=250$ to $\beta=1$ (charge-neutral polyelectrolyte-capsid complex), and $N_b=400$ to $\beta>1$ (overcharged capsid). The ratio of the contour length of the polyelectrolyte and the interior circumference of the capsid,

$$\gamma \equiv \frac{(N_b-1)\langle R_\mathrm{bb}^2\rangle^{1/2}}{2\pi R_\mathrm{c}}, \tag{10}$$

varies between 2 and 8. The volume fractions of polyelectrolyte beads inside the capsid correspond to 0.64%, 1.4%, and 2.6% for the three polyelectrolyte lengths considered.

The three angular force constants selected are $k_\mathrm{angle}=0.51\times 10^{-24}$, 10.8×10^{-24}, and 121×10^{-24} J deg^{-2}. These angular force constants correspond to the bare persistence lengths $l_p^0=8.5$, 50, and 550 Å, respectively, as evaluated for an uncharged polymer according to the relation $l_p^0=\langle R_\mathrm{bb}^2\rangle^{1/2}/(1+\langle\cos\alpha\rangle)$ [40]. The first value would be approximately appropriate for ssRNA and the last value would be appropriate for ds B-DNA. The ratio of the persistence length and the inner capsid radius

$$\delta \equiv \frac{l_p^0}{R_\mathrm{c}} \tag{11}$$

adopts the values $\delta\approx 0.2$, 1, and 11 for the three different bending stiffnesses considered.

D. Simulation details

The properties of the model systems were evaluated by performing Metropolis Monte Carlo (MC) simulations in the canonical ensemble. All interactions within the cell were considered; hence no potential cutoff was applied.

Four kinds of trial displacement were employed: (i) single-particle move, (ii) pivot rotation of a randomly selected part of the polyelectrolyte, (iii) slithering move of the polyelectrolyte, and (iv) translation of the polyelectrolyte (only applied to the polyelectrolyte solutions). The probability of the single-particle move was 100 times larger than those of the other types of trial displacements.

The acceptance rates of the different types of trial moves for an encapsidated polyelectrolyte are obviously lower than the corresponding rates in solution at the same set of displacement parameters. That gives rise to a lower equilibration rate for the encapsidated systems, in particular for large N_b and/or large l_p^0. To better assess the equilibrium structure, equilibration runs were performed with two different initial polyelectrolyte conformations: random and spool-like. In the latter conformation, all beads were placed on a spherical surface with radius 46 Å and with 9.5 Å separation between two adjoining strands and 6 Å separation between bonded beads. Results are given for random initial polyelectrolyte conformations, unless otherwise stated.

After an equilibration run involving 2×10^5 passes (attempted moves per particle), the production runs comprised typically $(6-10)\times 10^5$ passes. The reported uncertainties were calculated by dividing the total simulation into ten sub batches and are presented as one standard deviation of the mean. All simulations were carried out using the integrated Monte Carlo/molecular dynamics/Brownian dynamics simulation package MOLSIM [41].

E. Structural characterization

The structure of the polyelectrolyte was examined by computing the structure factor $S(\mathbf{q})$ for polyelectrolyte-associated beads according to

$$S(\mathbf{q}) = \left\langle \frac{1}{N_b}\left|\sum_{j=1}^{N_b}\exp(i\mathbf{q}\cdot\mathbf{r}_j)\right|^2\right\rangle \tag{12}$$

where $\mathbf{q}$ is the scattering vector, and $\mathbf{r}_j$ the position of the bead j with the limit $S(q\to 0)=N_b$, since all beads belong to the same chain.

We also evaluated the real-space radial density distribution $\rho(r)$ and the associated running coordination number $n_{rc}(r)=\int_0^r 4\pi r'^2\rho(r')dr'$. The former describes the particle number density at the radial distance r and the latter the number of particles within the radial distance r from the center of the cell with limits $n_{rc}(0)=0$ and $n_{rc}(R_\mathrm{cell})=N_i$.

Finally, in order to distinguish isotropic and spool-like polyelectrolyte structures, we evaluated the *toroidal parameter* τ defined as

$$\tau = \left\langle \frac{1}{N_b-2}\left[\sum_{\alpha=x,y,z}\left(\sum_{i=2}^{N_b-1}\frac{(\mathbf{r}_{i-1,i}\times\mathbf{r}_{i,i+1})_\alpha}{|\mathbf{r}_{i-1,i}\times\mathbf{r}_{i,i+1}|}\right)^2\right]^{1/2}\right\rangle \tag{13}$$

where $\mathbf{r}_{i-1,i}$ and $\mathbf{r}_{i,i+1}$ are the vectors of two successive bonds and × denotes a vector product. The toroidal parameter approaches 1 when the beads are arranged along an ideal toroid and fluctuates around $1/(N_b-2)$ for a disordered (random) distribution.

III. RESULTS

We will first discuss the results for the case of a polyelectrolyte-free capsid in the presence of its counterions. Then, we will turn to the results for capsids filled by polyelectrolyte molecules of variable length and stiffness. Finally, we examine the thermodynamics of the encapsidation process.

A. Polyelectrolyte-free capsid

Our model for a polyelectrolyte-free capsid is illustrated in Fig. 1 (top left). Recall that counterions are able to traverse the capsid, so the number of counterions inside the capsid is not a conserved quantity. The dependence of the counterion distribution on the cell volume was investigated by varying the cell radius over the interval $R_\mathrm{cell}=100-1000$ Å. Figure 2 displays the radial number density $\rho(r)$ and running coordination number $n_{rc}(r)$ for cell radii $R_\mathrm{cell}=100$ (solid curves) and 1000 Å (dashed curves) over the radial interval $r=0-100$ Å.

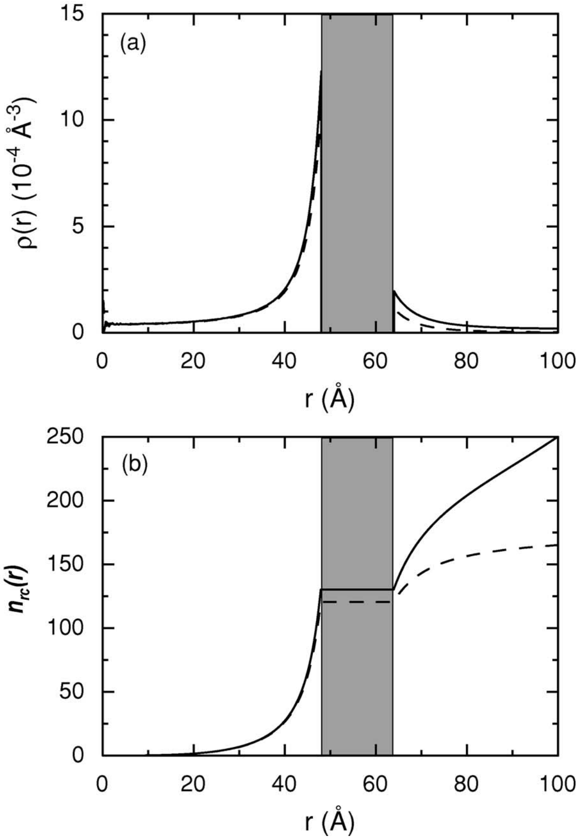

FIG. 2. Capsid counterion (a) number density $\rho(r)$ and (b) running coordination number $n_{rc}(r)$ as a function of the radial distance r for a polyelectrolyte-free capsid with cell radius $R_{\text{cell}}=100$ (solid curves) and 1000 Å (dashed curves). The shaded areas denote the location of the capsid.

Counterions are densely accumulated on the capsid surfaces and in particular on the inner one [Fig. 2(a)]. The contact density is five times larger at the inner surface as compared to the outer one. The stronger accumulation of counterions at the inner surface is mainly a consequence of the capsid charges being located closer to that surface. The value of the running coordination number at $r=R_c$ shows that ca. 50% of the counterions are residing inside the capsid [Fig. 2(b)]. It might be expected that number of interior counterions decreases with increasing cell size for entropic reasons, but a 1000-fold increase of the cell volume reduces the average number of counterions inside the capsid by only a small amount, from 130 to 121, and the counterion density profile *inside* the capsid is only marginally affected. However, the exterior counterion density is markedly reduced when the cell volume was increased, e.g., a 50% density decrease at 10 Å from the surface appeared. For the present capsid model we conclude that (i) the monovalent counterions are approximately equally partitioned inside and outside a polyelectrolyte-free capsid and (ii) the counterion partitioning is only very weakly dependent on the cell volume.

The effects of the position and representation of the capsid charges on the counterion distributions have also been examined. First, the radial position of the capsid charges has a considerable impact on the number of counterions inside the capsid. As the radial position of the capsid charges is shifted outward, the number of interior counterions decreases. For example, if the discrete capsid charges are located at 2 Å from the *outer* surface ($r=R_c+10$ Å), only 24% of the counterions remained inside the capsid. This response of the counterion distribution on the location of the capsid charges could be understood from the electrostatic potential energy, e.g., evaluated as the integral of the electrostatic field squared. The electrostatic field in the region between the inner and outer capsid surfaces becomes smaller *if* the counterions are predominantly located at the surface at which the capsid charges are residing.

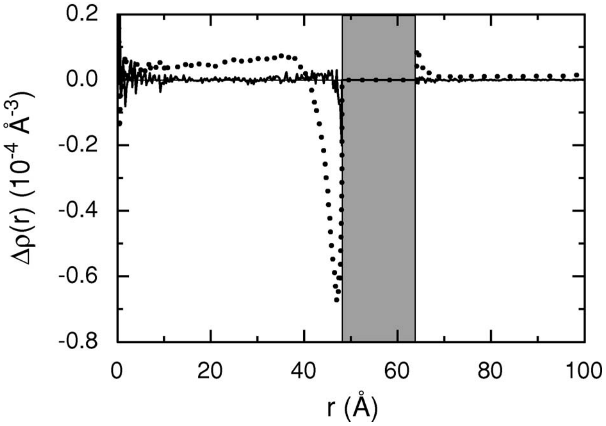

FIG. 3. Difference of capsid counterion number densities $\Delta\rho(r)$ as a function of the radial distance r for a polyelectrolyte-free capsid with a cell radius $R_{\text{cell}}=100$ Å, where $\Delta\rho(r)=l_p^0(r)-l_p^0(r)$ (solid curve) and $\Delta\rho(r)=\rho^{\text{h}}{}_{\text{PB}}(r)-\rho^{\text{h}}{}_{\text{MC}}(r)$ (dotted curve) with superscripts "h" and "d" denoting a homogeneous and a discrete capsid charge distribution, respectively, and the subscript referring to the numerical solution method (see text for more details). The shaded area denotes the location of the capsid.

Next, Fig. 3 (solid curve) shows that replacement of the discrete capsid charges by a homogeneously charged spherical surface located at same radial position as the discrete charges ($r=R_c+2$ Å) affect the counterion distribution very weakly. Only a small reduction of the counterion density near the inner capsid surface is observed. With a homogeneous spherical charge distribution, the electrostatic potential inside the capsid is truly constant. Hence, even the discrete capsid charge distribution generates a practically constant electrostatic potential inside the capsid. This is reasonable, since the distance between two neighboring capsid charges is only ≈10 Å and the charges are evenly distributed.

Finally, the counterion distribution has been determined by using the mean-field Poisson-Boltzmann (PB) equation for the case of a homogeneous spherical charge distribution. The predicted number of counterions inside the capsid is 127 as compared to 130 obtained from the MC simulation for the same model. Moreover, Fig. 3 (dotted curve) shows that the PB equation provides a reasonable distribution of the counterion density. The accumulation of counterions at the inner capsid surface is underestimated (e.g., 6% reduction of the contact density), and the counterion density is overestimated deeper in the interior. Thus, the partitioning and distribution of the monovalent counterions are well described by the PB equation.

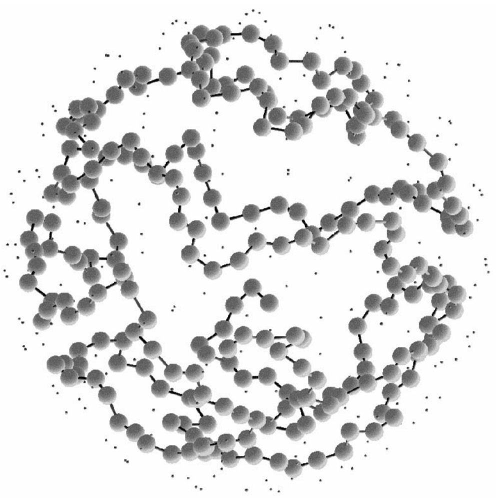

FIG. 4. Snapshot showing an encapsidaded polyelectrolyte consisting of N_b=250 beads with a bare persistence length l_p^0=8.5 Å (connected gray spheres) and the capsid charges (dots) taken from the end of the production simulation. The small ions are omitted for sake of clarity.

B. Polyelectrolyte-containing capsid

We will first consider a capsid containing the flexible polyelectrolyte of the intermediate length. It will be followed by an account of the effects of varying the polyelectrolyte length and the influence of the chain stiffness.

1. Flexible polyelectrolyte of intermediate length

The flexible polyelectrolyte (mimicking ssRNA) of intermediate length possesses N_b=250 beads and has the bare persistence length l_p^0=8.5 Å. The polyelectrolyte and the capsid have the same absolute charges, giving the charge ratio β=1, which will be referred to as the charge-neutral case. The contour length of the polyelectrolyte is about five times the circumference of the inner capsid surface, γ=5, and the bare persistence length is much smaller than the radius of the inner capsid surface, δ=0.2. Within the statistical uncertainty, the results for this system did not depend on the initial chain configuration.

Figure 4 displays a typical snapshot of the encapsidated polyelectrolyte molecule. The polyelectrolyte appears to be at the inner capsid surface. Moreover, the chain is locally well folded, which is supported by the average angle between consecutive beads being $\langle\alpha\rangle$=126° and much smaller than 180°. The toroidal parameter is small, τ=0.04.

The polyelectrolyte structure factor $S(q)$ is shown in Fig. 5 (solid curve). The weak maximum at $q \approx 1.3$ Å^{-1} is related to the to average spacing between bonded beads $d \approx \langle R_{\mathrm{bb}}^2\rangle^{1/2}$=5.8 Å by $d \approx 2\pi/q$. A sequence of sharp minima appears in the interval $q \approx 0.07-0.7$ Å^{-1}. The position of these minima agree with those of the form factor of a 10 Å thick homogeneous spherical shell centered at r=45 Å (dotted curve).

The radial number density of the beads is shown in Fig. 6(a). A prominent peak appears at the hard-sphere contact distance of the beads with the inner capsid surface (r=48 Å), and nearly all beads are in fact localized in a spherical layer of ≈10 Å thickness, in agreement with the structure factor analysis. The rms radius of gyration $\langle R_{\mathrm{G}}^2\rangle^{1/2}$=45.8 Å of the polyelectrolyte is consistent with the adsorption of the polyelectrolyte beads to the inner capsid surface.

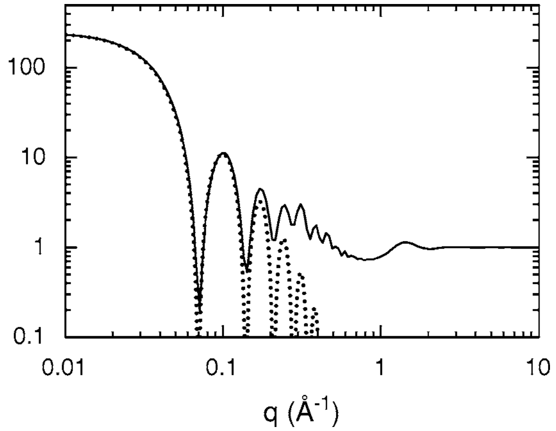

FIG. 5. Single-polyelectrolyte structure factor $S(q)$ as a function of the wave vector q in a log-log representation for an encapsidaded polyelectrolyte with N_b=250 beads and a bare persistence length l_p^0=8.5 Å with a cell radius R_{cell}=563.1 Å (solid curve). The form factor $P(q)$ for a spherical layer with the inner radius R_1=40 Å and the outer one R_2=50 Å, according to $P(q)=N_b\{3/[q^3(R_2{}^3-R_1{}^3)] \times[(qR_2)^2 j_1(qR_2)-(qR_1)^2 j_1(qR_1)]\}^2$ with j_1 denoting the spherical Bessel function of the first order, is also given (dotted curve).

The radial number densities of the small ions are also shown in Fig. 6. On average six of the 250 polyelectrolyte counterions resided inside the capsid, while practically none of the capsid counterions remained inside the capsid. The distribution of the polyelectrolyte counterions inside the capsid is fairly homogeneous with a maximum at r=40 Å and a depletion layer near the inner capsid surface [Fig. 6(a)]. This implies that the electrostatic potential is relatively uniform at $r<30$ Å even when the polyelectrolyte is present. Outside the capsid, capsid counterions are accumulated near the capsid surface, whereas polyelectrolyte counterions are depleted near the outer surface [Fig. 6(b)]. The small-ion density profiles level off and merged at $r \approx 300$ Å.

In summary, for the charge-neutral complex (β=1), the flexible polyelectrolyte is localized close to the inner capsid surface and locally folded with little lateral ordering and no spool-like arrangement. Since the electrostatic potential generated by the capsid charges is basically constant inside the capsid, the driving force for the adsorption of the polyelectrolyte at the inner surface must be mainly the electrostatic self-repulsion of the polyelectrolyte chain. The self-repulsion is however too weak to produce a lattice ordering (Wigner crystallization) at the inner surface.

The encapsidation process involves a substantial amount of *counterion release* from the both the polyelectrolyte and the capsid. Its thermodynamic consequences will be discussed in Sec. III C. Despite the zero charge of the complex (β=1), the number of polyelectrolyte counterions residing inside the capsid exceeds the number of capsid counterions. The weak accumulation of polyelectrolyte counterions at the inside surface of the bead layer originates from the deviation

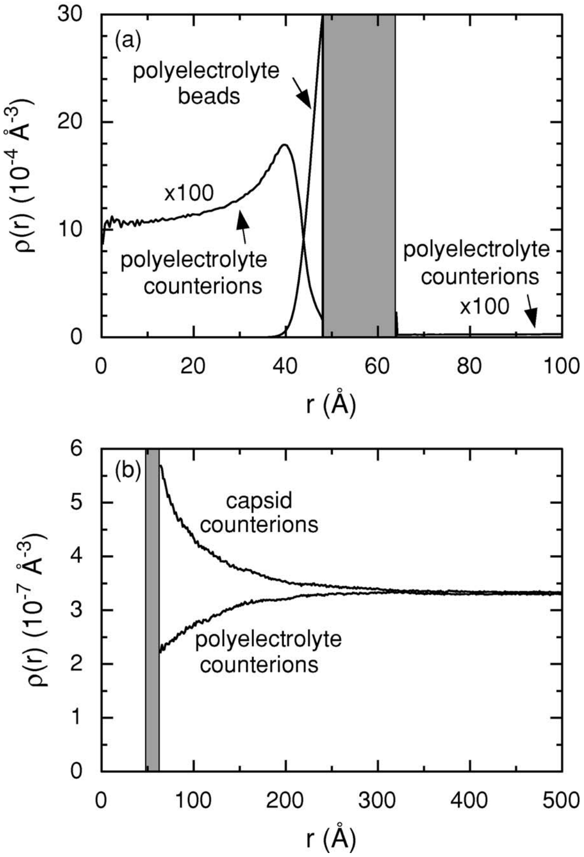

FIG. 6. Number density $\rho(r)$ of (a) beads and polyelectrolyte counterions and (b) polyelectrolyte counterions and capsid counterions as a function of the radial distance r for an encapsidaded polyelectrolyte with $N_b = 250$ beads and a bare persistence length $l_p^0 = 8.5$ Å with a cell radius $R_{\text{cell}} = 563.1$ Å. In (a), the density of the polyelectrolyte counterions is multiplied by 100.

of a nonspherical distribution of mainly the discrete polyelectrolyte charges enabling charge correlations. The accumulation of the (negatively charged) capsid counterions and the depletion of the (positively charged) polyelectrolyte counterions near the outer capsid surface is a consequence of the (positive) net charge of the polyelectrolyte-containing capsid when now also including the small ions inside the capsid.

To gain further insight into the effect of the capsid charges on the polyelectrolyte conformation, three simplified systems were investigated, in which the capsid is uncharged and its counterions are removed. In system I, both polyelectrolyte and polyelectrolyte counterions are confined inside the nonpermeable sphere (a similar system was recently studied by Pais *et al.* [42]). In system II, the capsid is permeable only to the polyelectrolyte counterions and the cell radius is $R_{\text{cell}} = 563.1$ Å. In system III, the capsid is again permeable for the polyelectrolyte counterions but with an infinite R_{cell}. Technically, system III was realized by having the polyelectrolyte confined in a sphere with no counterions present. At an infinite cell radius, all counterions are diluted away. In all three systems, the capsid had the same size as before and the polyelectrolyte possessed $N_b = 250$ beads and had the bare persistence length $l_p^0 = 8.5$ Å.

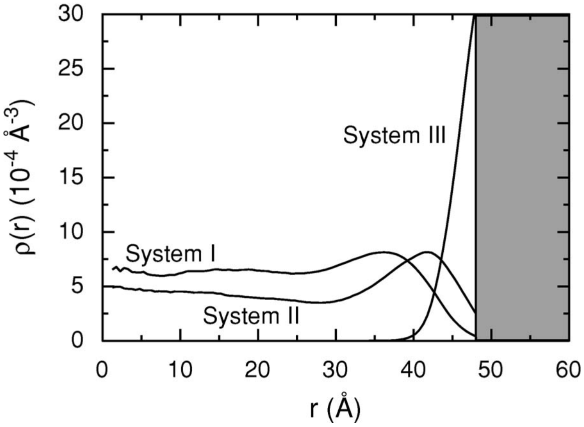

FIG. 7. Bead number density $\rho(r)$ as a function of the radial distance r for an *uncharged* spherical capsid confining one polyelectrolyte with $N_b = 250$ beads and a bare persistence length $l_p^0 = 8.5$ Å, where the capsid is nonpermeable for the polyelectrolyte counterions (system I), the capsid is permeable for polyelectrolyte counterions and a cell radius $R_{\text{cell}} = 563.1$ Å (system II), and the capsid is permeable for the polyelectrolyte counterions and infinite R_{cell} (system III).

Figure 7 shows the radial bead number densities of systems I–III. In the case of the impermeable capsid (system I), the beads are relatively homogeneously distributed over the spherical volume, with a weak density maximum at $r \approx 36$ Å and a depletion region near the surface of the sphere. For a semipermeable capsid with the finite R_{cell} (system II), the bead distribution remains fairly homogeneous but the density maximum is closer to the capsid surface ($r \approx 42$ Å) and more pronounced. Most of the polyelectrolyte counterions (184 of the 250) remain in the capsid. Finally, in the absence of any counterions (system III), the polyelectrolyte is strongly accumulated to the inner capsid surface, leaving a large void at $r < 40$ Å. Thus, we observe a successive displacement of the polyelectrolyte to the capsid surface at decreasing number of counterions residing inside the capsid, which is attributed to the reducing screening of the bead-bead repulsion. Eventually, when all counterions are diluted away a large central region inside the capsid becomes free of polyelectrolyte beads.

We can now assess the effect of the capsid charges on the polyelectrolyte distribution. First, a comparison of the bead density distributions for the charged capsid in Fig. 6 and the uncharged capsid (system II) in Fig. 7, at identical cell volume, shows that the presence of the capsid charges and capsid counterions triggers a strong adsorption of the polyelectrolyte beads on the inner capsid surface. Next, in fact the bead density distribution for the charged capsid in Fig. 6 is nearly identical to that for the uncharged capsid at infinite volume (system III) in Fig. 7. This should not come as a surprise, since in the former system only six polyelectrolyte counterions and no capsid counterions reside in the capsid, whereas in the latter system there are no small ions at all.

Hence, the adsorption of the polyelectrolyte onto the inner capsid surface is not due to a direct electrostatic attraction between polyelectrolyte and capsid charges. (The electrostatic potential inside the capsid originating from the capsid

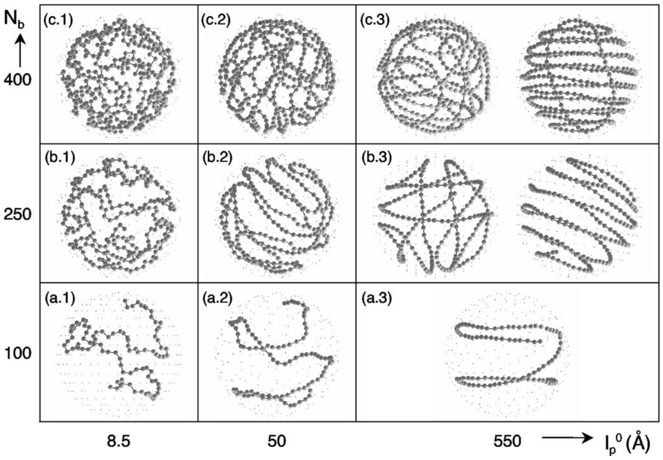

FIG. 8. Snapshots showing encapsidated polyelectrolyte beads (connected gray spheres) and capsid charges (dots) at increasing number of beads N_b (bottom to top) and increasing bare persistence length from l_p^0 (left to right) taken from the end of the production simulations. Same length scale is used among the panels. In (b.3) and (c.3), the right snapshots show final configuration obtained from simulations starting with a spool-like initial chain configuration. The small ions are omitted for sake of clarity.

charges is virtually constant.) Instead, we propose the following mechanism. Without capsid charges, the polyelectrolyte counterions are inside the capsid to match the polyelectrolyte charge and making the electrostatic field emancipating from the capsid small. When capsid charges are present, they replace the charge-matching function of the polyelectrolyte counterions. At $\beta=1$, the small ions now become (to the leading order) homogeneously distributed throughout the cell, which maximizes their entropy. Consequently, the introduction of the capsid charges and their counterions lead to a release of the polyelectrolyte counterions. Finally, since the screening among the polyelectrolyte beads by the polyelectrolyte counterions has vanished, the polyelectrolyte beads repel each other and by the geometrical constrain they become adsorbed onto the inner capsid surface.

2. Flexible polyelectrolytes of different length

Snapshots of the final configurations displaying the configuration of encapsidated polyelectrolytes and the position of the capsid charges for the nine systems with bead numbers $N_b=100$, 250, and 400 and bare persistence lengths $l_p^0=8.5$, 50, and 550 Å using random initial chain conformations are displayed in Fig. 8. Snapshots of using spool-like initial configurations are shown for two cases with $l_p^0=550$ Å (chains mimicking dsDNA). Single-chain structure factors $S(q)$, radial bead number densities $\rho(r)$, and normalized radial number densities of the small ions $\rho(r)/\rho_{\text{av}}$ with ρ_{av} denoting the average number density in the cell for each of the nine systems are presented in Figs. 9 and 10 and Figs. 11 and 12, respectively. Values of rms bead-to-bead separation $\langle R_{\text{bb}}^2\rangle^{1/2}$, mean angle between three consecutive beads $\langle\alpha\rangle$, rms radius of gyration $\langle R_{\text{G}}^2\rangle^{1/2}$, and toroidal parameter τ are compiled in Table II.

We will start to examine the effect of varying the polyelectrolyte length but maintaining the short bare persistence length. Recall that that three different polyelectrolyte lengths considered $N_b=100$, 250, and 400 correspond to polyelectrolyte-capsid charge ratios $\beta=0.4$, 1, and 1.6 and to polyelectrolyte-capsid size ratios $\gamma=1.9$, 2.7, and 7.6, respectively. No significant difference between the two different types of initial chain configurations could be detected for the flexible polyelectrolytes.

Figure 8 (first column) shows that in all three cases the polyelectrolyte is locally well folded and disordered. The smallest polyelectrolyte is too short to cover the capsid surface, whereas the coverage becomes more homogeneous with the longer chains. The toroidal parameter τ is quite small in all three cases (Table II), and indeed no spool formation is observed.

The corresponding structure factors shown in Fig. 9 (first column) are similar for the two longer polyelectrolytes, but

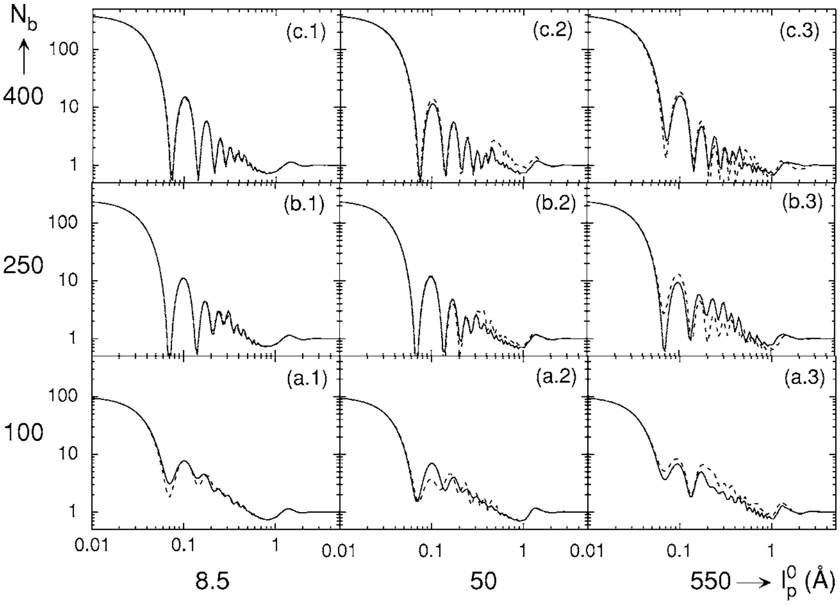

FIG. 9. Single-polyelectrolyte structure factor $S(q)$ as a function of the wave vector q in a log-log representation at increasing number of beads N_b (bottom to top) and increasing bare persistence length from l_p^0 (left to right) with random (solid curves) and spool-like (dashed curves) initial chain configuration.

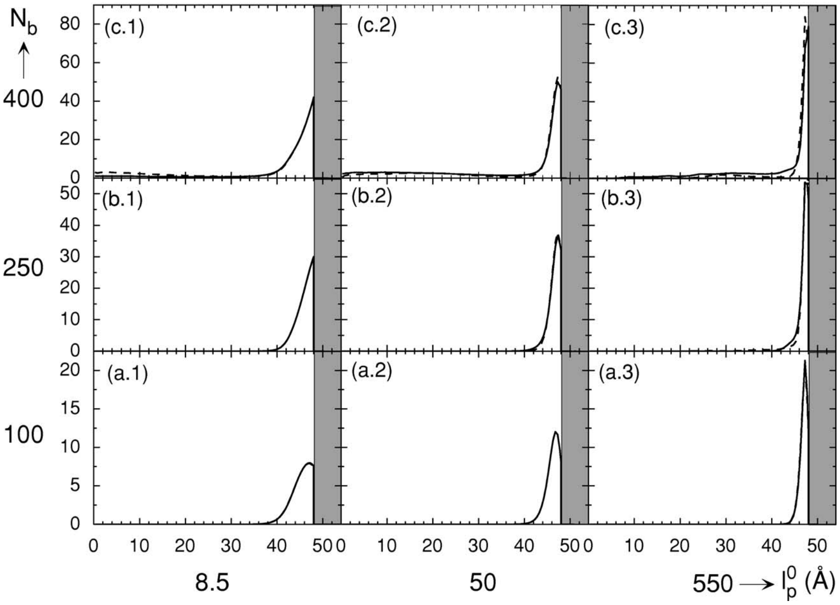

FIG. 10. Polyelectrolyte bead number density $\rho(r)$ (in units of 10^{-4} $Å^{-3}$) as a function of the radial distance r (in units of Å) at increasing number of beads N_b (bottom to top) and increasing bare persistence length from l_p^0 (left to right) with random (solid curves) and spool-like (dashed curves) initial chain configuration. The shaded areas denote the location of the capsid.

display less-developed minima for the shorter one. The latter is attributed to the poor coverage of the capsid surface leading to a larger heterogeneity of the local environment of a bead.

The bead number density distributions shown in Fig. 10 (first column) display that the two shorter polyelectrolytes are located within a 10 Å thick layer at the inner capsid surface. For the longest polyelectrolyte there is, apart from this surface layer, also a nearly uniform density involving about 25 beads distributed over the remaining part of the capsid interior. The density difference between the central region and the shell region is too large to significantly alter the form factor of a shell scattering model [43], in agreement with our numerical findings [cf. panels (b.1) and (c.1) of Fig. 9].

Figure 11(a.1) shows that for the case of an undercharged capsid (N_b=100, β=0.4), 48 capsid counterions reside inside the shell. The capsid counterion density near the inner surface is much larger than the density near the outer capsid surface, just as for the polyelectrolyte-free capsid (β=0; see Fig. 2). For the charge-neutral case (N_b=250, β=1), Fig. 11(b.1) shows that all of the capsid counterions have been released, as previously discussed. Finally, for the case an overcharged capsid (N_b=400, β=1.6) shown in Fig. 11(c.1), the capsid counterions are completely released and depleted in a zone extending ≈300 Å from the outer capsid surface. Panels (a.1) and (c.1) of Fig. 12 show that the distribution of the polyelectrolyte counterions basically is the reverse of that of the capsid counterions. For an undercharged capsid, a depletion zone appears outside the capsid, while for an overcharged capsid, the polyelectrolyte counterions are highly concentrated near the inner surface.

Thus, the main features of the encapsidated polyelectrolyte remains, but the distribution of the small ions varies among the undercharged, equal-charged, and overcharged cases. Nevertheless, noticeable is the presence of beads in

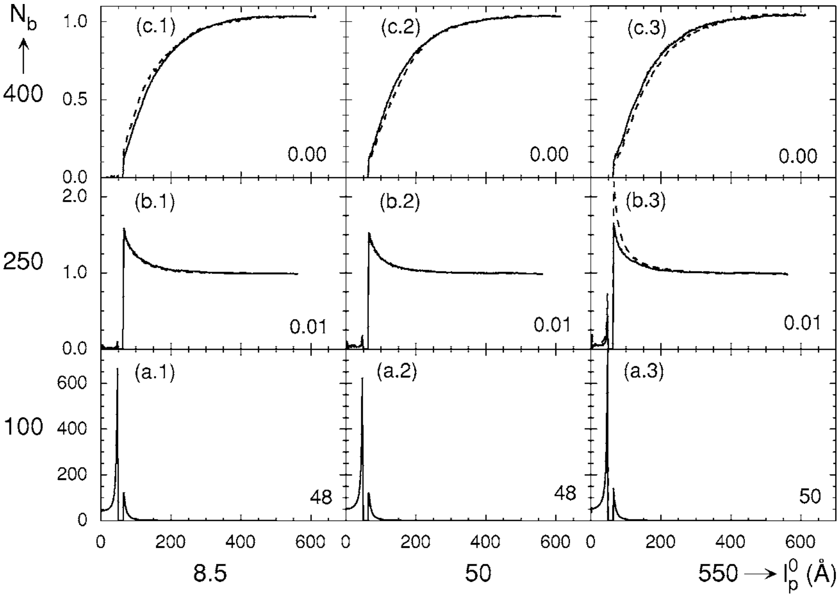

FIG. 11. Normalized capsid counterion number density $\rho(r)/\rho_{av}$ as a function of the radial distance r (in units of Å) at increasing number of beads N_b (bottom to top) and increasing bare persistence length from l_p^0 (left to right) with random (solid curves) and spool-like (dashed curves) initial chain configuration. The numbers of counterions inside the capsid are also given.

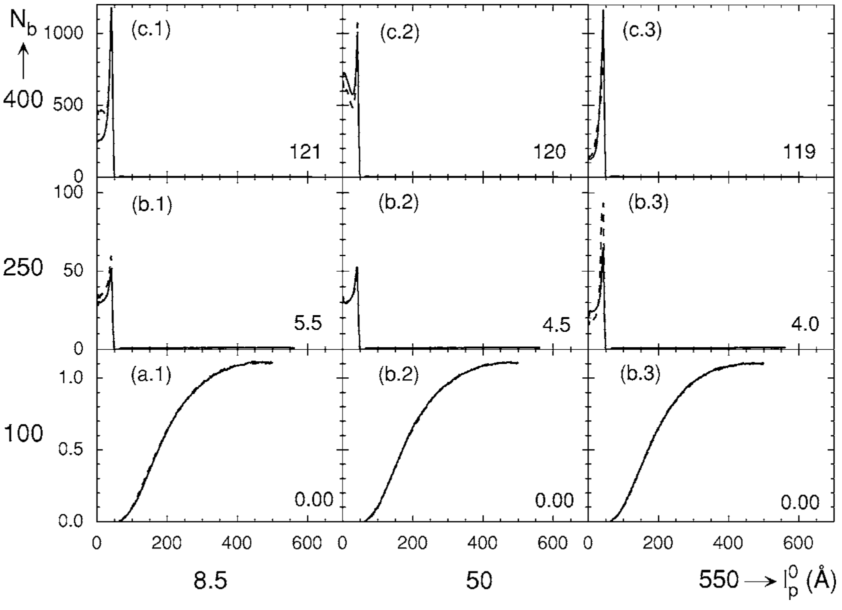

FIG. 12. Normalized polyelectrolyte counterion number density $\rho(r)/\rho_{\mathrm{av}}$ as a function of the radial distance r (in units of Å) at increasing number of beads N_b (bottom to top) and increasing bare persistence length from l_p^0 (left to right) with random (solid curves) and spool-like (dashed curves) initial chain configuration. The numbers of counterions inside the capsid are also given.

the capsid core for the longest chain. Naively, that seems to be reasonable in view of the fact that the ratio of the polyelectrolyte and capsid charges places us in the overcharging regime, so one could expect a part of the polyelectrolyte being not associated with the capsid.

It must, however, be recalled that the polyelectrolyte configuration does not directly depend on the capsid charge since the potential of the capsid charges is essentially uniform. To obtain a better physical insight, we turn again to the counterion distribution. First, for the polyelectrolyte-free capsid, carrying 250 elementary charges, about 125 counterions are inside the capsid [see Fig. 2(b)]. When the polyelectrolyte-capsid complex was undercharged ($N_b = 100$), 48 capsid counterions and no polyelectrolyte counterions remained inside the capsid. For the charge-neutral polyelectrolyte-capsid complex ($N_b=250$), only a few polyelectrolyte counterions remained inside the capsid. In none of these cases there are sufficient polyelectrolyte counterions inside the capsid to produce screening of the polyelectrolyte self-repulsion. However, when the polyelectrolyte-capsid complex is overcharged by 150 elementary charges ($N_b = 400$), 121 polyelectrolyte counterions remained inside the capsid. These counterions appear inside to compensate the charge of the overcharged capsid. It is the screening action of these counterions that facilitates some polyelectrolyte beads to reside in the capsid interior (though significantly less than 121). This result highlights the central role of the counterion distribution for the polyelectrolyte configuration.

TABLE II. Average properties of encapsidated polyelectrolytes: rms bead-to-bead separation $\langle R_{\mathrm{bb}}^2\rangle^{1/2}$, angle between three consecutive beads $\langle\alpha\rangle$, rms radius of gyration $\langle R_{\mathrm{G}}^2\rangle^{1/2}$, and the toroidal parameter τ defined by Eq. (13).

N_b	l_p^0 (Å)	$\langle R_{\mathrm{bb}}^2\rangle^{1/2}$ (Å)	$\langle\alpha\rangle$ (deg)	$\langle R_{\mathrm{G}}^2\rangle^{1/2}$ (Å)	τ
100	8.5	5.93(1)	128.4(1)	45.03(2)	0.072(3)
	50	5.84(1)	157.3(1)	45.90(3)	0.190(8)
	550	5.65(1)	170.5(1)	46.81(2)	0.651(3)
250	8.5	5.81(1)	125.5(1)	45.84(1)	0.040(1)
	50	5.75(1)	156.7(1)	46.42(1)	0.116(2)
	50[a]	5.71(1)	157.3(1)	46.56(1)	0.252(3)
	550	5.65(1)	168.9(1)	46.80(1)	0.160(5)
	550[a]	5.46(2)	170.2(1)	46.56(3)	0.586(2)
400	8.5	5.76(1)	119.7(1)	44.52(3)	0.035(1)
	50	5.65(1)	155.5(1)	44.66(3)	0.061(1)
	50[a]	5.66(1)	157.1(1)	45.05(2)	0.298(2)
	550	5.47(2)	169.3(3)	45.30(9)	0.38(5)
	550[a]	5.65(1)	169.8(1)	46.36(9)	0.69(1)

[a] From spool-like initial configuration.

Finally, we notice that the distribution of the small ions never is such that the net charge of the small ions inside the capsid compensates the net charge of the polyelectrolyte-capsid complex. The average net charge of the complex, including the small ions residing inside the capsid, equals $125e$, $52e$, $6e$, and $-29e$ for $\beta=0$, 0.4, 1, and 1.6, respectively. The remaining charge compensation appears by charges residing in a diffuse layer outside the capsid.

3. Polyelectrolyte flexibility

The role of polyelectrolyte flexibility will first be examined for the charge-neutral case ($\beta=1$). Thereafter, we will compare undercharged and overcharged capsids with polyelectrolytes of various flexibility.

Polyelectrolytes with the three different chain flexibilities corresponding to the bare persistence lengths $l_p^0=8.5$, 50, and 550 Å will be referred as to flexible, semi-flexible, and stiff, respectively. We recall that the ratio of the persistence and the inner capsid radius became $\delta\approx 0.2$, 1, and 11, respectively. Hence, we expect an enthalpic bending energy cost to affect the encapsidation. For the two stiffer chains, the simulation became more demanding and difficulties to achieve equilibrium arose as concluded from obtaining somewhat different results using different initial chain configurations.

However, we will argue that it is still possible to reach certain meaningful conclusions.

Figure 8 shows snapshots of final states for a random initial configuration [panels (b.2) and (b.3), left] and for a spool-like initial configuration [panel (b.3), right]. Both the semiflexible [Fig. 8(b.2)] and stiff [Fig. 8(b.3)] polyelectrolytes are locally extended, in contrast to the case of the flexible polyelectrolyte shown in Fig. 8(b.1). For the semiflexible polyelectrolyte, numerous rings appear which are connected by some sharp bends (referred to as U turns). The toroidal parameter is low, $\tau = 0.12$, due to these U turns. For the case of a spool-like initial configuration, a single spool emerged without any U turns (snapshot is not shown) and the toroidal parameter is increased to $\tau = 0.25$. The mean angle between three consecutive beads becomes $\langle \alpha \rangle \approx 157°$ for both initial chain configurations, which indicates that still some local bending fluctuations appear.

For the stiff polyelectrolyte with a random initial configuration [Fig. 8(b.3), left] the final configuration is similar to that for the semiflexible polyelectrolyte except for a higher degree of local order. In the case of a spool-like initial configuration [Fig. 8(b.3), right], the final state is a well-organized spool structure consisting of a number of concentric rings without U turns. The two ends of the polyelectrolyte are located at the two poles of the spool and the toroidal order parameter $\tau = 0.59$ is achieved. The mean potential energies for the random and spool-like initial configurations are $U/N_b kT = 2.8$ and 2.1, respectively. With the conjecture that the polyelectrolyte enthalpy (from the bending energy) dominates over the polyelectrolyte entropy (associated with the polyelectrolyte configurational fluctuations), we propose that the structure obtained with the initial spool-like configuration is the one closest to the equilibrium one. In fact, such a "ground-state assumption" has been found to work well for the adsorption of stiff polyelectrolytes on oppositely charged macroions [44].

Despite this lack of ergodicity in terms of the toroidal order, the structure factors of the final states of the semiflexible and stiff polyelectrolytes are nearly independent of the initial configuration, and resemble that of the flexible polyelectrolyte [cf. panels (b.2) and (b.3) with panel (b.1) of Fig. 9]. The radial bead density distributions showed that the thickness of the bead layer decreased when the polyelectrolyte stiffness was increased (Fig. 10). For the stiff chain, the layer width is about one bead (≈3 Å). The thickness of the bead layer is marginally larger for the random initial configurations (solid curves) than for the spool-like initial configurations (dashed curves), presumably because the U turns lead to some chain crossings. We also notice that the differences among the radial density distributions [panels (b.1), (b.2), and (b.3) of Fig. 10] are obviously too small to significantly affect the form factor [43]. The number of counterions inside the capsid and their radial number distribution also are only marginally affected by the chain stiffness and the initial chain configuration [panels (b.1), (b.2), and (b.3) of Figs. 11 and 12].

We now continue with semiflexible and stiff chains away from charge neutrality ($\beta \neq 1$). For the short polyelectrolyte ($N_b = 100$ and $\beta = 0.4$), full ergodicity was achieved, while for the longer polyelectrolyte ($N_b = 400$ and $\beta = 1.6$), we encountered a similar dependence on the initial configurations as for $N_b = 250$.

The encapidated short and stiff polyelectrolyte forms two parallel rings separated by a transition region [Fig. 8(a.3)] consistent with $\gamma = 1.9$. The two rings are approximately symmetric with respect to a mirror plane that passes through the center of the capsid. A similar structure can be discerned for the short and semiflexible polyelectrolyte, although considerable fluctuations are visible as well [Fig. 8(a.2)]. For the long and stiff chain and a random initial configuration, we obtained a final structure that is characterized by a large number of U turns [Fig. 8(c.3), left]. For a spool-like initial configuration, we encountered two separate organizational motifs. The majority of the beads are part of a spool structure being in close contact to the inner capsid surface, while a minority of the beads is organized in an inner ring oriented perpendicularly with respect to the spool [Fig. 8(c.3), right]. We regard the inner ring as a seed for the formation of a second spool. The spacing between adjacent turns in the spool is smaller as for chains of intermediate length. Using mean potential energies and the ground-state approximation as above, we again reach the conclusion that the spool structure is likely to describe the free energy minimum for the stiff and long polyelectrolyte.

Also for undercharged and overcharged capsids, the structure factors given in Fig. 9 display only a weak dependence on the stiffness.

The radial number density distributions shown in panels (c.1), (c.2), and (c.3) of Fig. 10 supports our earlier observation that the beads of the longest encapsidated polyelectrolyte are only partly adsorbed on the inner capsid surface, irrespectively of the polyelectrolyte stiffness. As for the intermediate chain length, the different number of chain crossings inside the surface layer obtained for the two different types of initial chain configurations affects the radial densities again only very little [panels (c.2) and (c.3) of Fig. 10].

Finally, Figs. 11 and 12 show that the distributions of the small ions are again insensitive to the polyelectrolyte flexibility, for both $\beta = 0.4$ and 1.6.

Our central conclusion is that (i) the radial distribution of the beads inside the capsid and the distribution of the counterions are essentially independent of the polyelectrolyte flexibility, but (ii) the lateral organization of the beads is sensitively dependent on it. The fact that the radial density distribution and the structure factor of both bead and counterions are not very sensitive to the initial chain configuration suggests that, despite the nonergodicity of our simulations for stiffer chains, we still may be able to use our results for a study of the thermodynamics of the polyelectrolyte-capsid interaction.

C. Thermodynamics of polyelectrolyte encapsidation

The analysis of the thermodynamics of polyelectrolyte encapsidation is based on the scenario outlined in Fig. 1. The encapsidation free energy was obtained as the free energy difference between an initial state composed of separated polyelectrolyte-free capsid and polyelectrolyte solutions and a final state representing a solution of a polyelectrolyte-

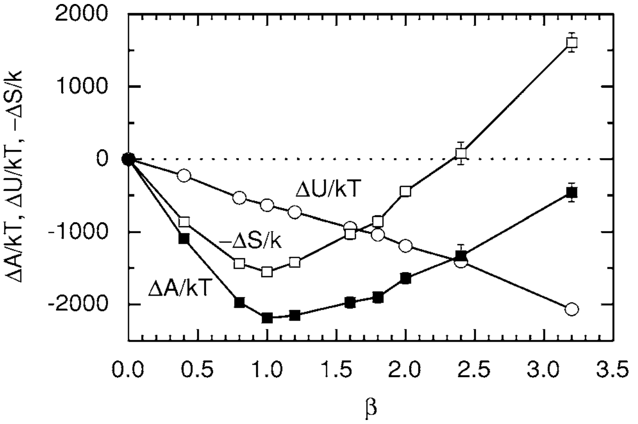

FIG. 13. Change in reduced free energy $\Delta A/kT$, reduced enthalpy $\Delta U/kT$, and reduced entropy $-\Delta S/k$ for the polyelectrolyte encapsidation process shown in Fig. 1 and evaluated as described in Appendix B as a function of the ratio of the polyelectrolyte and capsid charges β at the bare persistence length $l_p^0=8.5$ Å.

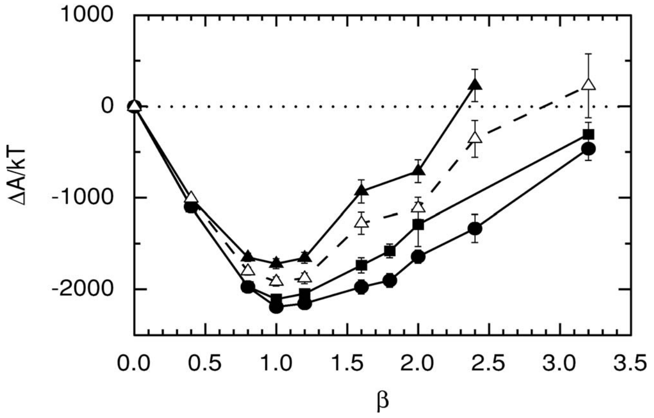

FIG. 14. Change in reduced free energy $\Delta A/kT$ for the polyelectrolyte encapsidation process shown in Fig. 1 and evaluated as described in Appendix B as a function of the ratio of the polyelectrolyte and capsid charges β at the bare persistence lengths $l_p^0=8.5$ (circles), 50 (squares), and 550 Å (triangles). Results obtained using random (filled symbols and solid lines) and spool-like (open symbols and dashed lines) initial chain conformations in the CP systems are given.

containing capsid. The procedure of evaluating the free-energy difference is discussed in Appendix B.

Figure 13 displays the free energy change for the flexible polyelectrolyte as a function of the ratio of the polyelectrolyte and capsid charges ranging from $\beta=0$ to 3.2. Results are only given for random initial configuration, since no differences were detected between results obtained for the two procedures of generating initial chain configurations.

The free energy change $\Delta A(\beta)$ is negative over the β range investigated. Of course, we have no information on the barrier of the penetration of the polyelectrolyte into the capsid, since the encapsidation path is not addressed here. Next, $\Delta A(\beta)$ possesses a minimum at, or near, the charge-neutral point ($\beta=1$) with $\Delta A(\beta=1)\approx-2200kT$, which corresponds to $-8.8kT$ per bead. Between $\beta=0$ and 1, $\Delta A(\beta)$ decreased nearly linearly, whereas at $\beta>1$ the increase became more gradual leading to $\Delta A(\beta)\approx-450kT$ at $\beta=3.2$ and it can be assumed by extrapolation that $\Delta A(\beta)\approx 0kT$ at $\beta=3.5$. Hence, for the flexible polyelectrolyte (i) the total electrostatic free energy of the final encapsidated state is lower than that of the initial state, implying that the encapsidation is thermodynamically favored, until the polyelectrolyte charge is about is ≈ 3.5 times that of the capsid charge and (ii) the encapsidation free energy gain is maximized for a charge-neutral polyelectrolyte-capsid complex.

The enthalpic ΔU and entropic ΔS contributions to ΔA are also displayed in Fig. 13. The enthalpy change $\Delta U(\beta)$ is negative throughout and approximately a *linear* function of β. This linearity indicates that ΔU is dominated by the difference in electrostatic energy due to the potential difference of single beads appearing in a polyelectrolyte solution and inside the capsid. The long-range bead-bead electrostatic repulsion, which would have a nonlinear dependence on β, apparently plays only a secondary role.

The encapsidation entropy change $\Delta S(\beta)$ is positive [$-\Delta S(\beta)$ negative] for $\beta \leqslant 2.4$; hence the encapsidation is entropically favored for this range of β. The β dependence of $-\Delta S(\beta)$ and $\Delta A(\beta)$ is similar and $-\Delta S(\beta)$ also displayed a minimum at $\beta\approx 1$. From the crossings of ΔU and ΔS, we find the encapsidation predominantly entropy driven for $\beta<1.7$ and enthalpy driven for $1.7<\beta<3.2$. Physically, the increase in entropy upon encapsidation is due to the release of capsid and polyelectrolyte counterions that are associated with them in the initial state. Neglecting secondary effects, this entropy increase becomes maximized for $\beta=1$, since *all* counterions can be released for a charge-neutral complex. When $\beta\neq 1$, some counterions remain inside or near the capsid to compensate for the net charge of the polyelectrolyte-capsid complex. This claim can be verified by making a first-order estimate of $\Delta S_{\text{estimate}}(\beta=1)/k$. The assumptions that (i) relative volumes of the regions of free and trapped counterions are 10^3 and (ii) 50% of the counterions (both polyelectrolyte and capsid counterions) are trapped in the initial state and none in the final state give $\Delta S_{\text{estimate}}/k\approx 0.5(250+250)\ln(10^3)\approx 1700$, which is in qualitative agreement with the simulation results. In this view, at $\beta=2.4$ where $\Delta S\approx 0$ the entropy gain associated with the release of the capsid counterions and some polyelectrolyte counterions are balanced by the entropy cost of confining the other polyelectrolyte counterions inside the capsid. At larger β, the entropy cost of confining an increasing number of polyelectrolyte counterions dominates over the approximately constant entropy gain associated with the release of the other small ions.

Figure 14 compares the encapsidation free energy of polyelectrolytes with different stiffness as a function of the charge ratio β. For the case of the stiff polyelectrolyte results are given for random and spool-like initial conformations, since a statistical significant dependence on the initial chain configurations is found. However, the function $\Delta A(\beta)$ for the two are were similar and their difference is generally smaller than the effect of the chain stiffness.

Three important observations that can be deduced from Fig. 14 are (i) the encapsidation free energy gain is reduced as the polyelectrolyte becomes stiffer, (ii) the reduction of the free-energy gain due to stiffness is relatively small, and (iii) the minimum of $\Delta A(\beta)$ is around $\beta \approx 1$ regardless of the chain stiffness. At $\beta \approx 1$, $\Delta A/kT$ increases from ca. -2200 to ca. -1900 as the persistence length is increased from 8.5 to 550 Å. This free energy change could be compared with the average angular potential energy change $\Delta U_{\text{angle}}/kTN_b = 0.77$ and 2.44 for $l_p^0 = 8.5$ and 550 Å, respectively, for the encapsidation process. Hence, the increase in ΔA by $\approx 1.2kT$ per bead corresponded to the larger strain of $1.7kT$ per bead induced in the stiff polyelectrolyte upon the encapsidation.

IV. DISCUSSION AND CONCLUSION

We have investigated the structure of capsid-enclosed viral polyelectrolytes and the thermodynamics of the encapsidation process by performing MC simulations on a simplified model system. In the following, we will review our main conclusions and confront them with theoretical predictions of polyelectrolyte encapsidation based on the DH approximation.

The key conclusions of our study are as follows.

(i) The encapsidated chain is adsorbed onto the inner capsid surface, not by direct electrostatic attraction to the capsid charges, but through a self-repulsion among the polyelectrolyte charges. The conformation of encapsidated chains undergo a dramatic reorganization at increasing bare persistence length as monitored by toroidal order parameter τ. For low intrinsic stiffness, the chain configuration is essentially laterally disordered, while with increasing stiffness the chain adopted a spool-like structure that resembles the dsDNA configuration observed for phage viruses. Our results indicate the possibility of a sharp transition from a disordered to spool-like structure at increasing polyelectrolyte stiffness.

(ii) For undercharged capsids ($\beta < 1$) and for moderately overcharged capsids ($1 < \beta < 2.4$) encapsidation is favored both enthalpically and entropically. The entropy increase is due to a net release of small ions. For stronger overcharged capsids ($\beta > 2.4$) encapsidation still is enthalpically favored, but entropically disfavored. For even stronger overcharged capsids ($\beta > 3.5$) the entropy penalty becomes larger than the enthalpy gain and the encapsidation ceases to be thermodynamically favorable.

(iii) The encapsidation free energy gain per polyelectrolyte monomer is maximized when polyelectrolyte and capsid charges fully neutralized each other ($\beta = 1$).

(iv) The chain stiffness affects only weakly the thermodynamics, despite its strong structural effects.

The third conclusion would have interesting consequences in the context of the life cycle of a virus. Suppose a viral genome was progressively packed into a partially filled capsid. As the number of packed monomers increased, the addition of successive monomers would continue to lower the free energy, provided the number of beads was such that the complex remained undercharged ($\beta < 1$). Polyelectrolyte packaging would be a thermodynamically spontaneous process in this regime. For an overcharged complex ($\beta > 1$), the addition of a monomer would increase the free energy of the system, i.e., this would not be a spontaneous process. Hence, *if* we envision the encapsidation process as a passive step-by-step loading process it would not continue past the charge-neutral point. However, the total encapsidation free energy will remain negative as long as the number of beads is less than about 3.5 times the number of capsid charges ($\beta < 3.5$). Therefore, at least theoretically, a cooperative capsid self-assembly and genome confinement can give rise to overcharged capsids.

Our simplified model neglects some important features of $T=3$ viruses, which makes it difficult to confrontation our data with experimental viral assembly studies. First, important characteristics of $T=3$ viruses scale differently upon a size reduction. Second, we considered the salt-free limit; at physiological salt conditions, the added salt screens (weaken) the electrostatic interactions. Both issues affect quantitatively the free energy change in a way, but not qualitatively. Nonetheless it can be mentioned that the structural studies of self-assembling $T=3$ ssRNA viruses report that the charge of the encapsidated polyelectrolyte typically lies in the range of $-3500e$ to $-4000e$ [37]. If we compare this to the typical capsid charge of about $+1800e$ to $+2300e$ [32], we must conclude that typical $T=3$ ssRNA viruses are actually highly *over* charged. Confusingly, *in vitro* studies of the encapsidation of short homopolymer ssRNA strands in CCMV capsids by Bancroft [45], using sedimentation methods, report that the encapsidated RNA charge corresponds to about $-1500e$, which is lower than the capsid charge of about $+2000e$. A separate *in vitro* study of the self-assembly of hepatitis B virus with shorter RNA sequences also appears to produce packing fractions that are significantly lower than that of those of actual viral genome, though this was not established on a quantitative basis [9].

It is interesting to compare the results of our model with the theory of van der Schoot and Bruinsma based on the DH approximation [32] and applied to encapsidation at finite salt concentrations. They obtained a dependence of the encapsidation free energy on the number of monomers that resembled Fig. 14; however, with the minimum located at a polyelectrolyte charge twice that of the capsid. Overcharging is in fact a well-known feature of polyelectrolyte adsorption on oppositely charged surfaces [46–51]. The physical explanation of this phenomenon is based on the idea that only a fraction of the charged monomers are involved in the charge neutralization of the oppositely charged surface, the remaining ones are electrostatic screening by the added salt ions. It would seem that the *in vivo* charge and size of the polyelectrolyte of $T=3$ ssRNA viruses can be better accounted for by the DH description with added salt, whereas *in vitro* self-assembly with shorter RNA sequences is in closer accord with the results of the present model without salt.

The structural results of our model also can be compared with the theory by van der Schoot and Bruinsma [32] by focusing on the bead density profile. We found that for the charge ratio $\beta < 1$, all beads are essentially adsorbed on the inner capsid surface, while the core of the capsid was empty. In the overcharged regime, $\beta > 1$, the density was high near the capsid surface and low and relatively uniform in the interior. On the other hand, the theory predicted for packing fraction at or near the free-energy minimum that the genome density should exhibit a radial power-law dependence extending into the capsid interior. The RNA density profiles of

TABLE III. Polyelectrolyte properties determined from simulation of a polyelectrolyte and monovalent counterions confined in prolate-shaped cell at bead number density $\rho_b = 5.11 \times 10^{-7}$ Å^{-3}: rms bead-to-bead separation $\langle R_{\text{bb}}^2 \rangle^{1/2}$, angle between three consecutive beads $\langle \alpha \rangle$, rms end-to-end distance $\langle R_{ee}^2 \rangle^{1/2}$, rms components of the gyration tensor along the principal axes $\langle G_{xx}^2 \rangle^{1/2}$, $\langle G_{yy}^2 \rangle^{1/2}$, and $\langle G_{zz}^2 \rangle^{1/2}$ ($G_{xx} \leq G_{yy} \leq G_{zz}$), and shape factor $\langle R_{ee}^2 \rangle / \langle R_{\text{G}}^2 \rangle$.

N_b	Major axis[a] (Å)	l_p^0 (Å)	$\langle R_{\text{bb}}^2 \rangle^{1/2}$ (Å)	$\langle \alpha \rangle$ (deg)	$\langle R_{ee}^2 \rangle^{1/2}$ (Å)	$\langle G_{xx}^2 \rangle^{1/2}$ (Å)	$\langle G_{yy}^2 \rangle^{1/2}$ (Å)	$\langle G_{zz}^2 \rangle^{1/2}$ (Å)	$\langle R_{ee}^2 \rangle / \langle R_{\text{G}}^2 \rangle$
100	750	8.5	6.09(1)	130.7(2)	335(5)	11.3(3)	27(1)	105(2)	9.3(1)
		50	6.08(1)	158.0(1)	426(7)	12.6(5)	33(2)	132(2)	9.5(2)
		550	6.07(1)	172.8(1)	536(5)	9.3(3)	25(2)	160(2)	10.9(1)
250	1875	8.5	6.12(1)	132.1(2)	885(23)	23(2)	58(5)	271(8)	10.1(0.2)
		50	6.09(1)	158.1(1)	1137(21)	27(2)	45(4)	341(8)	10.8(0.1)
		550	6.08(2)	172.8(1)	1273(13)	24(2)	67(2)	375(4)	11.1(0.1)
400	3000	8.5	6.11(1)	131.7(2)	1443(13)	36(3)	54(2)	426(3)	11.2(0.1)
		50	6.07(1)	158.0(1)	1575(16)	47(3)	91(2)	464(4)	11.0(0.2)
		550	6.07(2)	172.7(1)	1885(43)	32(2)	80(2)	533(11)	12.2(0.2)

[a] Length of minor axes $R_x = R_y = 250$ Å.

$T=3$ ssRNA viruses measured by x-ray diffraction report that the RNA density is high and relatively constant, apart from a nearly empty core with a radius of about 10 nm [7,52]. These features appear to be better reproduced by our model than by the DH-based theory.

Finally, we will argue that the main origin for the difference between the locations of the minimum of the free energy with respect to polyelectrolyte-capsid charge ratio obtained in the present paper and in van der Schoot and Bruinsma [32] originates in differences between the two systems that were investigated. We believe that the screening length–capsid size ratio plays a fundamental role in this respect. In particular, in the present system there was no added salt. (Whether a screening length can be defined for a system without added salt is dubious.) Under these conditions the free energy cost of forming a system where the net charge of the polyelectrolyte-capsid complex deviates significantly from zero is significantly enhanced. On the other hand, in the work by van der Schoot and Bruinsma [32] the Debye screening length was small compared to the capsid size. Hence, polyelectrolyte charges inside the capsid that are located far from the capsid surface were screened by the added salt ions, while these charges are still contribute to the charge balance of the complex. This is perhaps better illustrated by comparison with the adsorption of polyelectrolytes onto a planar and oppositely charged surface [53]. If the salt concentration is low—and the Debye screening length large—then the adsorbed amount is to the first order controlled by charge neutralization, whereas at higher salt concentrations the polyelectrolyte charge exceeds that of the surface. The physical reason is again that the outer part of the adsorbed polyelectrolyte layer is electrostatically decoupled from the surface by electrostatic screening.

ACKNOWLEDGMENTS

Valuable discussions with Håkan Wennerström, Bill Gelbart, and Toan Nguyen are gratefully acknowledged. This work was supported by grants from the Swedish Research Council (VR) and by the National Science Foundation DMR Grant No. 0404507.

APPENDIX A: PROLATE-SHAPED CELL FOR POLYELECTROLYTE SOLUTION

Properties of polyelectrolyte solutions are approximated with those of a polyelectrolyte and its counterions confined in a prolate-shaped cell. In this appendix some details of the selection of the prolate shape and polyelectrolyte properties are provided.

The cell volume is determined by the polyelectrolyte density of the solution. Here, a dilute polyelectrolyte solution with a bead number density $\rho_{\text{b}} = 5.11 \times 10^{-7}$ $Å^{-3}$ is selected. The cell shape should ideally mimic the shape of the polyelectrolyte. The large linear charge density of the polyelectrolyte and the presence of monovalent counterions only lead to an extended polyelectrolyte, suggesting a prolate-shaped cell. Auxiliary simulations showed that polyelectrolyte properties in a prolate-shaped cell of constant volume is insensitive to (i) the length of the major axis R_z, provided it is larger than half the polyelectrolyte contour length, and (ii) the minor axes R_x and R_y, provide they are larger than ≈100 Å.

Prolate-shaped cells with minor axes $R_x = R_y = 250$ Å and the major axis R_z adjusted to the selected bead number density (Table III) were employed for the nine different polyelectrolyte solutions. Polyelectrolyte properties such as rms end-to-end distance, rms components of the gyration tensor along the principal axes, and a shape factor are collected in Table III. The rms value of the intermediate component of the gyration tensor $\langle G_{yy}^2 \rangle^{1/2}$ is at most 90 Å and thus much smaller than the minor axes. Moreover, R_z exceeded by at least fourfold the rms values of the largest component of gyration tensor $\langle G_{zz}^2 \rangle^{1/2}$. Hence, beside the indirect effect of confining the counterions, we consider the hard-sphere surfaces of the confining cell to have only a marginal effect on the polyelectrolyte configuration at the selected ρ_b.

Table III also provides some other properties of the polyelectrolytes. Noticeably, is the approximately linear increase of the rms end-to-end separation at increasing number of beads and the more extended shape as deduced from the shape factor at increasing bare persistence length. Extensive simulations of polyelectrolyte properties in polyelectrolyte solutions have been made by Stevens and Kremer [54].

APPENDIX B: FREE ENERGY CHANGE OF POLYELECTROLYTE ENCAPSIDATION

The procedure for the calculation of the free energy change of the polyelectrolyte encapsidation as depicted in Fig. 1 will be described in this appendix. The initial state contains two separated systems, one involving a polyelectrolyte-free capsid with its counterions in a spherical cell (C), and one involving a polyelectrolyte with its counterions in a prolate-shaped cell (P). In the final system, the polyelectrolyte is enforced to be inside the capsid, whereas the small ions may explore the full spherical cell (CP).

The calculation of the free energy of the polyelectrolyte encapsidation ΔA is facilitated by introducing decoupled states of the three systems, in which only the hard-core interactions remain [38]. Thus, ΔA can be expressed as a sum of three terms

$$\Delta A = \Delta A_1 + \Delta A_2 + \Delta A_3 \tag{B1}$$

with

$$\begin{aligned}\Delta A_1 = -\Delta A_{\mathrm{C}} - \Delta A_{\mathrm{P}} = -[A_{\mathrm{C}}(\text{coupled}) - A_{\mathrm{C}}(\text{uncoupled})]\\ -[A_{\mathrm{P}}(\text{coupled}) - A_{\mathrm{P}}(\text{uncoupled})],\end{aligned} \tag{B2}$$

$$\Delta A_3 = \Delta A_{\mathrm{CP}} = A_{\mathrm{CP}}(\text{coupled}) - A_{\mathrm{CP}}(\text{uncoupled}), \tag{B3}$$

where ΔA_1 denotes the free energy change of decoupling the C and P systems, ΔA_2 the free energy of mixing the decoupled C and P systems into the decoupled CP system, and ΔA_3 the energy change of coupling the CP system.

The free energy difference between the coupled and the decoupled states of a system can be evaluated by a coupling integration according to

$$\Delta A \equiv A(1) - A(0) \equiv \int_0^1 \frac{\partial}{\partial \lambda} A(\lambda) d\lambda = \int_0^1 \left\langle \frac{\partial}{\partial \lambda} U(\lambda) \right\rangle_\lambda d\lambda \tag{B4}$$

where the coupling parameter λ denotes a path from the decoupled ($\lambda=0$) to the coupled ($\lambda=1$) state described by $U(\lambda)$ and $\langle \cdots \rangle$ denotes a canonical ensemble average. In the present study, the path obtained by replacing e^2 with $(\lambda e)^2$ in Eqs. (3) and (4) k_{bond} with $\lambda^9 k_{\mathrm{bond}}$ in Eq. (5), and k_{ang} with $\lambda^6 k_{\mathrm{ang}}$ in Eq. (6), which produced reasonably smooth integrands in Eq. (B4), was used. The integral was evaluated by using the trapezoidal rule with 13 λ values.

The free energy term ΔA_2 in Eq. (B1) describes the free energy change of mixing two hard-sphere solutions subjected to one constraint. It can be divided into an ideal and a hard-sphere contribution according to

$$\Delta A_2 = \Delta A_2^{\mathrm{ideal}} + \Delta A_2^{\mathrm{HS}}. \tag{B5}$$

By considering the hard spheres originating from the polyelectrolyte beads and the small ions as distinguishable, we have

$$\begin{aligned}\frac{\Delta A_2^{\mathrm{ideal}}}{kT} &= -N_b \ln(V_{\mathrm{CP}}^{\mathrm{int}}) - (N_{\mathrm{cion,C}} + N_{\mathrm{cion,P}})\ln(V_{\mathrm{CP}})\\ &\quad - [-N_{\mathrm{cion,C}} \ln(V_{\mathrm{C}}) - (N_b + N_{\mathrm{cion,P}})\ln(V_{\mathrm{P}})]\\ &= -N_b \ln\left(\frac{V_{\mathrm{CP}}^{\mathrm{int}}}{V_{\mathrm{P}}}\right) + \left[-N_{\mathrm{cion,C}} \ln\left(\frac{V_{\mathrm{CP}}}{V_{\mathrm{C}}}\right)\right.\\ &\quad \left. - N_{\mathrm{cion,P}} \ln\left(\frac{V_{\mathrm{CP}}}{V_{\mathrm{P}}}\right)\right]\end{aligned} \tag{B6}$$

where N_b, $N_{\mathrm{cion,C}}$, and $N_{\mathrm{cion,P}}$ represent the numbers of beads, capsid counterions, and polyelectrolyte counterions, respectively, V_{C} and V_{P} are the cell volumes of the initial systems, V_{CP} is the cell volume of the final system (for the sake of simplicity the volume occupied by the capsid is neglected), $V_{\mathrm{CP}}^{\mathrm{int}}$ is the interior volume of the capsid, and k is Boltzmann's constant. In Eq. (B6), the first term in the last expression represents the compression of the (now) ideal unconnected beads into the capsid and the second one the free energy change of mixing two ideal solutions.

The second term in Eq. (B5) denotes the excess hard-sphere contribution. Using the Carnahan-Starling equation [55], it can be expressed according to

$$\begin{aligned}\frac{\Delta A_2^{\mathrm{HS}}}{kT} &= [\Delta A^{\mathrm{CS}}(N_{\mathrm{int}}, \eta_{\mathrm{int}}) + \Delta A^{\mathrm{CS}}(N_{\mathrm{ext}}, \eta_{\mathrm{ext}})] - [\Delta A^{\mathrm{CS}}(N_b\\ &\quad + N_{\mathrm{cion,P}}, \eta_{\mathrm{P}}) + \Delta A^{\mathrm{CS}}(N_{\mathrm{cion,C}}, \eta_{\mathrm{C}})]\end{aligned} \tag{B7}$$

with

$$\Delta A^{\mathrm{CS}}(N, \eta) = N \frac{\eta(4 - 3\eta)}{1 - \eta} \tag{B8}$$

where N_{int} and N_{ext} are the number of hard spheres inside and outside the capsid, η_{int} and η_{ext} the hard-sphere volume fractions inside and outside the capsid, and η_{P} and η_{C} the hard-sphere volume fractions in the two initial systems.

There is one final complication regarding the CP system. Because the hard spheres originating from the polyelectrolytes are confined in the capsid, the density of the hard spheres originating from the small ions will not be equal inside and outside the capsid. Hence, the distribution of particles entering in Eqs. (B5)–(B8) needs formally to be determined by a free energy minimization.

At the present conditions, the value of ΔA_2^{HS} ($<0.1kT$) and the change in $\Delta A_2^{\mathrm{ideal}}$ due to the abovementioned redistribution ($<1kT$) are smaller than the statistical uncertainties in $\Delta A_1 + \Delta A_3$, making these two issues less important. Hence, the approximation $\Delta A_2 \approx \Delta A_2^{\mathrm{ideal}}$ is sufficient.

[1] L. W. Enquist, R. M. Krug, V. R. Racaniello, A. M. Skalka, S. J. Flint, and S. J. Flint, *Principles of Virology: Molecular Biology, Pathogenesis, and Control* (ASM Press, Washington, DC, 2000).

[2] L. Tang, K. N. Johnson, L. A. Ball, T. Lin, M. Yeager, and J. E. Johnson, Nat. Struct. Biol. **8**, 77 (2001).

[3] H. H. Bink and C. W. Pleij, Arch. Virol. **147**, 2261 (2002).

[4] L. Liljas, K. Fridborg, K. Valegård, M. Bundule, and P. Pumpens, J. Mol. Biol. **244**, 279 (1994).

[5] K. Tars, M. Bundule, K. Fridborg, and L. Liljas, J. Mol. Biol. **271**, 759 (1997).

[6] K. Tars, K. Fridborg, M. Bundule, and L. Liljas, Virology **272**, 331 (2000).

[7] H. Tsuruta, V. S. Reddy, W. R. Wikoff, and J. E. Johnson, J. Mol. Biol. **284**, 1998 (1998).

[8] H. Fraenkel-Conrat and R. Williams, Proc. Natl. Acad. Sci. U.S.A. **41**, 690 (1955).

[9] P. Ceres and A. Zlotnick, Biochemistry **41**, 11525 (2002).

[10] J. M. Johnson, J. Tang, Y. Nyame, D. Willits, M. J. Young, and A. Zlotnick, Nano Lett. **5**, 765 (2005).

[11] V. S. Reddy, B. Natarajan, B. Okerberg, K. Li, K. Damodaran, R. T. Morton, C. L. Brooks III, and J. E. Johnson, J. Virol. **75**, 11943 (2001).

[12] W. C. Earnshaw and S. C. Harisson, Nature (London) **268**, 598 (1977).

[13] S. C. Riemer and V. A. Bloomfield, Biopolymers **17**, 785 (1978).

[14] R. W. Hendrix, Proc. Natl. Acad. Sci. U.S.A. **75**, 4779 (1978).

[15] S. C. Harrison, J. Mol. Biol. **171**, 577 (1978).

[16] J. Lepault, J. Dubochet, W. Baschong, and E. Kellenberger, EMBO J. **6**, 1507 (1987).

[17] M. E. Cerritelli, N. Cheng, A. H. Rosenberg, C. E. McPherson, F. P. Booy, and A. C. Steven, Cell **91**, 271 (1997).

[18] I. S. Garasvili, A. Y. Grosberg, D. V. Kuznetov, and G. M. Mrevlishvili, Biophysics (Engl. Transl.) **36**, 782 (1991).

[19] A. Fokine, P. R. Chipman, P. G. Leiman, V. V. Mesyanzhinov, V. B. Rao, and M. G. Rossmann, Proc. Natl. Acad. Sci. U.S.A. **101**, 6003 (2004).

[20] J. Kindt, S. Tzlil, A. Ben-Shaul, and W. M. Gelbart, Proc. Natl. Acad. Sci. U.S.A. **98**, 13671 (2001).

[21] S. Tzlil, J. T. Kindt, W. M. Gelbart, and A. Ben-Shaul, Biophys. J. **84**, 1616 (2003).

[22] P. K. Purohit, J. Kondev, and R. Phillips, Proc. Natl. Acad. Sci. U.S.A. **100**, 3173 (2003).

[23] T. Odijk, Biophys. J. **75**, 1223 (1998).

[24] P. K. Purohit, M. M. Inamdar, P. D. Grayson, T. M. Squires, and J. Kondev, Biophys. J. **88**, 851 (2005).

[25] D. Marenduzzo and C. Micheletti, J. Mol. Biol. **330**, 485 (2003).

[26] D. E. Smith, S. J. Tans, S. B. Smith, S. Grimes, D. L. Anderson, and C. Bustamante, Nature (London) **413**, 748 (2001).

[27] Y. R. Chemla, K. Aathavan, J. Michaelis, S. Grimes, P. J. Jardine, D. L. Anderson, and C. Bustamante, Cell **122**, 683 (2005).

[28] A. Evilevitch, M. Castelnovo, C. M. Knobler, and W. M. Gelbart, J. Phys. Chem. B **108**, 6838 (2004).

[29] A. Evilevitch, J. W. Gober, M. Philips, C. M. Knobler, and W. M. Gelbart, Biophys. J. **88**, 751 (2005).

[30] A. Cordova, M. Deserno, W. M. Gelbart, and A. Ben-Shaul, Biophys. J. **85**, 70 (2003).

[31] T. Odijk, Philos. Trans. R. Soc. London, Ser. A **362**, 1497 (2004).

[32] P. v. d. Shoot and R. Bruinsma, Phys. Rev. E **71**, 061928 (2005).

[33] J. Arsuaga, R. K.-Z. Tan, M. Vasquez, D. Sumners, and S. C. Harvey, Biophys. Chem. **101–102**, 475 (2002).

[34] J. Arsuaga, M. Vazquez, S. Trigueros, D. Sumners, and J. Roca, Proc. Natl. Acad. Sci. U.S.A. **99**, 5373 (2002).

[35] J. C. LaMarque, T. L. Le, and S. C. Harvey, Biopolymers **73**, 348 (2004).

[36] A. J. Spakowitz and Z.-G. Wang, Biophys. J. **88**, 3912 (2005).

[37] D. Zhang, R. Konecny, N. A. Baker, and J. A. McCammon, Biopolymers **75**, 323 (2004).

[38] T. Wallin and P. Linse, Langmuir **12**, 305 (1996).

[39] P. Linse, in *Advanced Computer Simulation Methods in Soft Matter Sciences*, edited by C. Holm and K. Kremer (Springer, Berlin, 2005), Vol. 185, p. 111.

[40] A. Akinchina and P. Linse, Macromolecules **35**, 5183 (2002).

[41] P. Linse, MOLSIM, Version 4.0, Lund University, Sweden (2004).

[42] A. A. C. C. Pais, M. G. Miguel, P. Linse, and B. Lindman, J. Chem. Phys. **117**, 1385 (2002).

[43] J. Wagner, J. Appl. Crystallogr. **37**, 750 (2004).

[44] H. Boroudjeridi and R. R. Netz, Europhys. Lett. **71**, 1022 (2005).

[45] J. B. Bancroft, E. Hiebert, and C. E. Braker, Virology **39**, 924 (1969).

[46] M. Jonsson and P. Linse, J. Chem. Phys. **115**, 10975 (2001).

[47] T. Wallin and P. Linse, J. Chem. Phys. **109**, 5089 (1998).

[48] T. T. Nguyen and B. I. Shklovskii, J. Chem. Phys. **114**, 5905 (2001).

[49] S. Y. Park, R. F. Bruinsma, and W. M. Gelbart, Europhys. Lett. **46**, 454 (1999).

[50] R. R. Netz and D. Andelman, Phys. Rep. **380**, 1 (2003).

[51] R. R. Netz and J. F. Joanny, Macromolecules **32**, 9013 (1999).

[52] A. Zlotnick, N. Cheng, S. J. Stahl, J. F. Conway, A. C. Steven, and P. T. Wingfield, Proc. Natl. Acad. Sci. U.S.A. **94**, 9556 (1997).

[53] J. F. Joanny, Eur. Phys. J. B **9**, 117 (1999).

[54] M. J. Stevens and K. Kremer, J. Chem. Phys. **103**, 1669 (1995).

[55] N. F. Carnahan and K. E. Sterling, J. Chem. Phys. **51**, 635 (1969).